



Cite this: *CrystEngComm*, 2020, 22, 2537

Quaternary phase diagrams as a tool for ionic cocrystallization: the case of a solid solution between a racemic and enantiopure ionic cocrystal†

Lixing Song,  Fucheng Leng, Koen Robeyns  and Tom Leyssens*

Received 6th February 2020,
Accepted 18th March 2020

DOI: 10.1039/d0ce00179a

rsc.li/crystengcomm

In this study, a general isothermal quaternary phase diagram of etiracetam (racemate)–levetiracetam (*S*-enantiomer)–CaCl₂·2H₂O–water is generated to understand the crystallization thermodynamics of ionic cocrystal systems. Solubility surface is depicted clearly by the appliance of contour lines and various polyhedrons of the domains in the IQPD are delineated according to the eutectic points. The system shows a full solid solution between the racemic and enantiopure ionic cocrystals.

Introduction

Cocrystals form a sub-class of multi-component systems.¹ When at least one component is an active pharmaceutical ingredient (API) and the other is pharmaceutically acceptable, the term pharmaceutical cocrystal is used.² Cocrystallization provides an attractive pharmaceutical formulation route especially for non-ionizable APIs which are not suitable for salt formation.^{3–6} Cocrystals have been shown to improve physicochemical properties of compounds in the pharmaceutical industry (*e.g.* solubility, thermal stability, intrinsic dissolution rate and hygroscopicity, *etc.*) without breaking the compound's internal structure or compromising its pharmacological activity.^{7–13} Ionic cocrystals (ICCs)^{14,15} are a special case of cocrystals, as they typically include a neutral organic molecule and an inorganic salt in a defined stoichiometric ratio.

Chirality in organic cocrystal systems has been extensively studied.^{16,17} Based on the properties of these systems, chiral resolution crystallization processes have been developed.^{18,19} Some recent contributions extend these studies to include ICCs. Resolution was shown to occur at the solid state for ICCs²⁰ due to the chiral selectivity of certain metals. Li⁺ selectively links with amino acids of a given handedness,²¹ which leads to the formation of conglomerates or racemic crystals constituted of homochiral chains. In the work done by our group, we furthermore highlighted the possibility of using the stoichiometry of the cocrystal as a reversible switch

for altering between a thermodynamically stable racemic compound and a conglomerate.²²

Levetiracetam²³ (LEV, (*S*)-2-(2-oxopyrrolidin-1-yl)butanamide, Fig. 1) is an anti-epileptic drug developed by Union Chimique Belge (UCB S.A.) that was approved by the Food and Drug Administration in 1999. Etiracetam²⁴ (ETI) is its racemic counterpart. Cocrystallization of both ETI and LEV have been intensively studied by our group. In our latest work, we reported a diverse ionic cocrystallization landscape of both LEV and ETI with the inorganic salts CaCl₂ and MgCl₂.²⁵ We showed homochiral preference during the cocrystallization process between ETI and CaCl₂, which means that homochiral chains are observed in the crystal structure of the racemic compound, similar to the chains observed in the enantiopure LEV counterpart.

In our contribution, we focused on understanding the solid state, relying purely on a mechanochemical approach to access ICC phases on a mg scale. To produce ICCs on a larger scale, solution-based crystallization processes are industrially more interesting. To control these processes, both underlying thermodynamics and kinetics need to be understood. For the former, phase diagrams (PDs) are key tools. They supply information about the nature and composition of the thermodynamically stable phases for a given overall composition under a constant pressure and temperature.²⁶ PDs of organic cocrystals have been reported to be decisive when

Institute of Condensed Matter and Nanosciences, Université Catholique de Louvain, Place Louis Pasteur 1, B-1348 Louvain-La-Neuve, Belgium.

E-mail: tom.leyssens@uclouvain.be

† Electronic supplementary information (ESI) available: pdf of additional experimental data, XRPD and phase diagram images; a small animation showing how the quaternary system is constructed from the different zones shown in Fig. 9. See DOI: 10.1039/d0ce00179a

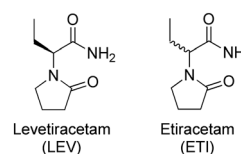


Fig. 1 The chemical structure of LEV and ETI.

developing a robust cocrystallization process.^{27–31} Recently, we showed how to develop such diagrams for ICCs, and how to apply them for the upscaling process of the piracetam–CaCl₂ ICC.³² In this contribution, we extend this work to include chirality, with the ultimate purpose to give guidelines toward the use of ICCs in the context of crystallization based chiral resolution. The PDs that need to be considered in this context, show the increasing complexity of both enantiomers being present, leading to quaternary phase diagrams (QPDs).^{33,34} Description and development of such a QPD has not yet been reported for ICCs. In this work, we are the first to do so, focusing on the ETI–LEV–CaCl₂·2H₂O–H₂O system.

Materials and methods

Starting materials

LEV was purchased from Xiamen Top Health Biochem Tech. Co. Ltd. ETI was prepared by racemization of LEV. 10 g of LEV together with catalytic amount (0.05 eq.) of MeONa were added to 10 mL of methanol. The solution was refluxed under continuous stirring for 24 h, and then cooled to room temperature. The compound crystallizes spontaneously. After filtration, the product was washed twice with methanol. The recovered product was used as such.³⁵ All the other reagents were purchased from Sigma and used without further purification.

Liquid assisting grinding (LAG)

Powder samples can be obtained mechanochemically through LAG of different stoichiometric mixtures of LEV or ETI and CaCl₂, with the addition of 10 μL of methanol. The sample was ground in a RETSCH Mixer Mill MM 400 for 90 min with a beating frequency of 30 Hz.

X-Ray powder diffraction (XRPD)

X-ray powder diffraction data were collected with a Siemens D5000 diffractometer equipped with a Cu X-ray source operating at 40 kV and 40 mA and the secondary monochromator allowing to select the K α radiation of Cu ($\lambda = 1.5418 \text{ \AA}$). A scanning range of 2θ values from 5° to 50° at a scan rate of 0.6° min⁻¹ was applied.

Phase diagram construction

Every solid–liquid phase diagram in solution discussed in this contribution was performed at a fixed temperature of 25 °C under atmospheric pressure. They were determined by creating a series of suspensions with different compositions of ETI, LEV and CaCl₂ in water according to the section of the quaternary diagram considered. The suspensions were seeded with all possible crystalline forms and stirred at 25 °C for over 48 h to make sure that the system reached thermodynamic equilibrium. The solid phases were recovered and analysed by XRPD. Solubility lines were determined by repeating the samples and adding water to the suspension up until complete dissolution. Water was added with 30 μL increments over a time period of 30 min, allowing for the achievement of thermodynamic

equilibration between each addition. This technique has been described elsewhere for the piracetam–CaCl₂–water system showing accurate results in the case of ICCs.³² PDs were drawn using ProSim Ternary Diagram software.

Results and discussion

As reported elsewhere,²⁵ ETI and LEV form dihydrate cocrystals with CaCl₂, namely ETI₂·CaCl₂·2H₂O (ICC1) and LEV₂·CaCl₂·2H₂O (ICC2). Both ICCs are quasi-isostructural and ICC1 reveals a homochiral packing around the Ca²⁺ cation. Combining different ratios of ICC1 and ICC2 always lead to similar XRPD patterns, which are also obtained when grinding from the starting materials (Fig. S1†).

Full quaternary phase diagram

Working under a given temperature and pressure, the system still allows for variation in amount of both enantiomers, cofomer and solvent. A full (isobaric and isothermal) quaternary phase diagram (IQPD) would be required for the description of such a system. IQPDs can be graphically represented by a 3D tetrahedron in which each vertex represents a pure component (solvent H₂O, the *S*-enantiomer LEV, the racemic compound ETI, and the pure salt CaCl₂·2H₂O).[‡] Anhydrous CaCl₂ is hygroscopic and spontaneously transforms into a dihydrate under ambient conditions. We therefore decided to start with the dihydrated CaCl₂·2H₂O at the vertex. Situations with a sub-stoichiometric amount of water are out of the scope of this contribution, as water is also used as the crystallization solvent.

As shown in Fig. 2, the four faces of the tetrahedron are isothermal ternary phase diagrams (TPDs). The first plane (highlighted in Fig. 3) represents the ternary solid-state phase diagram for ETI, LEV and CaCl₂·2H₂O. The second plane (highlighted in Fig. 4) corresponds to the TPD involving the ETI and CaCl₂·2H₂O cocrystal system in H₂O. The third plane, highlighted in Fig. 5, corresponds to the TPD of a cocrystal system, involving the *S*-enantiomer (LEV), the cofomer CaCl₂·2H₂O and H₂O. The fourth plane of the tetrahedron, highlighted in Fig. 6, represents the TPD involving a racemic (ETI) and enantiopure compound (LEV) in H₂O. Each of these TPDs will be discussed briefly below.

Solid-state TPD ETI–LEV–CaCl₂·2H₂O

The first ternary diagram developed is the solid-state TPD typically placed at the bottom of the tetrahedron shown in Fig. 3. In the context of this work, the diagram was built experimentally through a series of LAG experiments.§ A and

‡ One could consider placing the *R*-enantiomer at the vertex of the QPD instead of ETI. However, as the system is fully symmetrical, we decided to place ETI at the vertex.

§ Phase diagrams represent the most stable phase. Care has to be taken when constructing these solid-state diagrams through LAG as kinetic phases can be accessible. In this case, cross seeding experiments were performed as well as longer grinding times, always leading to similar conclusions.

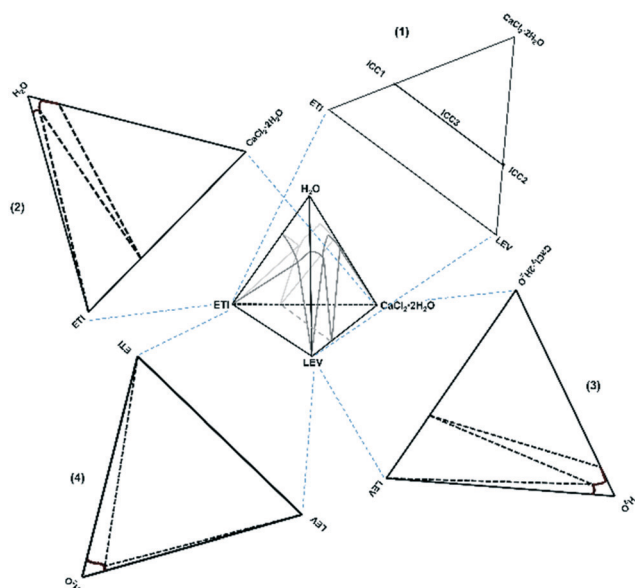


Fig. 2 General IQPD of a four-component system involving a racemic compound (ETI), a single enantiomer (LEV), a salt ($\text{CaCl}_2 \cdot 2\text{H}_2\text{O}$) and a solvent (H_2O).

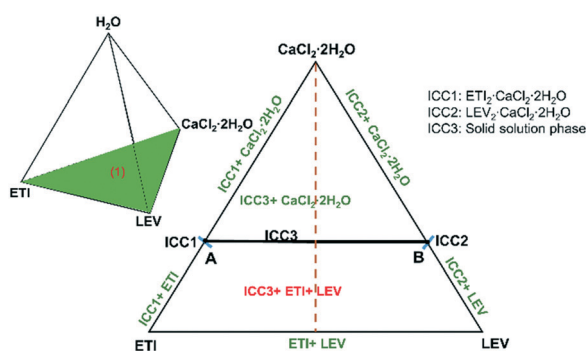


Fig. 3 Solid-state TPD for ETI-LEV- $\text{CaCl}_2 \cdot 2\text{H}_2\text{O}$ system. Pure phases are indicated in black, mixtures of two solid phases in green, and mixtures of three solid phases in red.

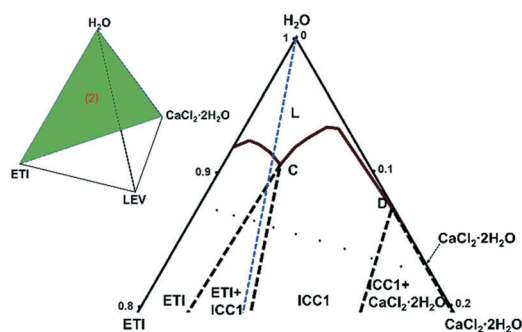


Fig. 4 Enlarged upper part of TPD for ETI- $\text{CaCl}_2 \cdot 2\text{H}_2\text{O}$ - H_2O system. Points C and D are eutectic points. Solid lines are solubility curves; separate dots indicate the composition of a series of starting suspensions and broken lines help visualize the different stability zones. The blue line shows the cocrystal stoichiometric line.

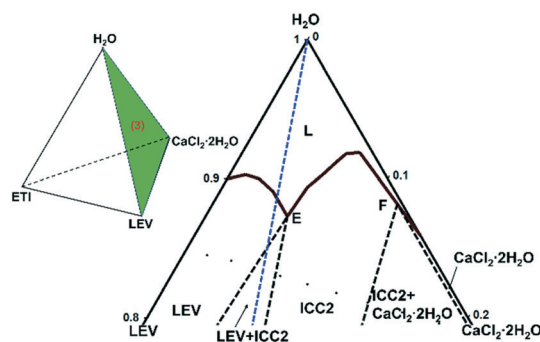


Fig. 5 Enlarged upper part of TPD for LEV- $\text{CaCl}_2 \cdot 2\text{H}_2\text{O}$ - H_2O system. Points E and F are eutectic points. Solid lines are solubility curves; separate dots indicate the composition of a series of starting suspensions and broken lines help visualize the different stability zones. The blue line shows the cocrystal stoichiometric line.

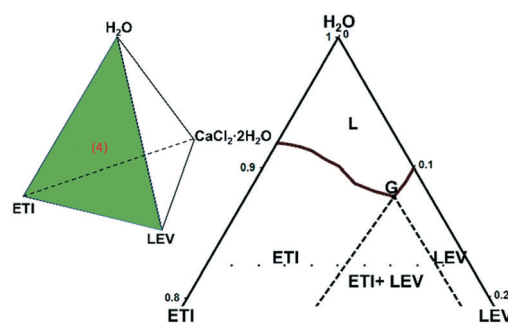


Fig. 6 Enlarged upper part of TPD involving ETI and LEV in water. Solid lines are solubility curves; separate dots indicate the composition of a series of starting suspensions and broken lines help visualize the different stability zones.

B represent the fully racemic ICC1 and enantiopure ICC2 cocrystal respectively. Sides of the diagram contain mixtures of two different phases (in green): mixtures of ETI and LEV on the bottom and mixtures of ICC and starting materials depending on stoichiometric conditions on the left and right sides. Starting with a 50/50 mixture of *RS*-ETI (1 equiv.) and *S*-ETI (1 equiv.), gradual addition of $\text{CaCl}_2 \cdot 2\text{H}_2\text{O}$ is represented by the orange dashed line. Initially a triphasic region appears with excess ETI and LEV and a single ICC phase corresponding to the solid solution of ICC1 and ICC2 (which will be termed as ICC3). Addition of $\text{CaCl}_2 \cdot 2\text{H}_2\text{O}$ (0.5 equiv.) leads to full transformation to the solid solution form ICC3 and a further addition of $\text{CaCl}_2 \cdot 2\text{H}_2\text{O}$ leads to a biphasic region consisting of this latter and the solid solution. Understanding the solid phase diagram is important as they highlight the combination of solid phases that can be obtained in a thermodynamically stable manner in suspension.

TPDs ETI (or LEV)- $\text{CaCl}_2 \cdot 2\text{H}_2\text{O}$ - H_2O systems

We then introduced the solvent, first creating the isothermal TPD of ETI/LEV- $\text{CaCl}_2 \cdot 2\text{H}_2\text{O}$ - H_2O . Experimental data (Tables S1 and S2[†] for the diagram involving ETI, Tables S3 and S4[†]

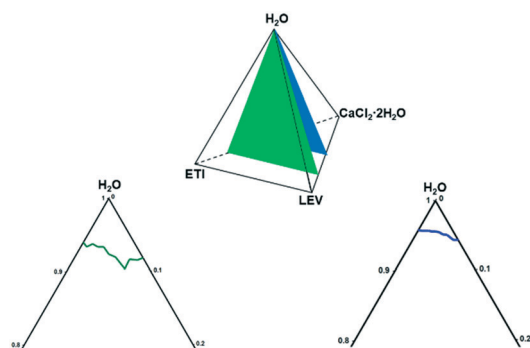


Fig. 7 Up: Schematic image of isoplethal planes. Down: Dissolution lines of two isoplethal planes. The left (green) one corresponds to the 3:1 plane and the right (blue) one to the 1:1 plane.

for the diagram involving LEV) is represented graphically in respectively Fig. 4 and 5 (full version is shown in Fig. S2 and S3[†]). As expected, the system involving the enantiopure compound parallels the one of the racemic compound with a slightly higher solubility for the enantiopure compound (LEV). From these figures, the solubility of ETI and LEV in water at 25 °C are estimated at 0.83 g mL⁻¹ and 1.05 g mL⁻¹ respectively. In both cases, one clearly observes a relatively large zone where the ICC is stable in suspension. However, the stoichiometric line (2:1 blue line) does not cross this zone, meaning that these cocrystals do not behave congruently in water at 25 °C. When suspending cocrystals in water, the system will spontaneously evolve to a mixture of cocrystal and ETI or LEV, or to a pure ETI or LEV, according to the amount of solvent present. Therefore, preparation of pure ICCs by solution cocrystallization requires an excess amount of CaCl₂·2H₂O.

TPD ETI–LEV–H₂O system

The enlarged TPD involving ETI and LEV in water is shown in Fig. 6 (full version shown in Fig. S4;[†] experimental data

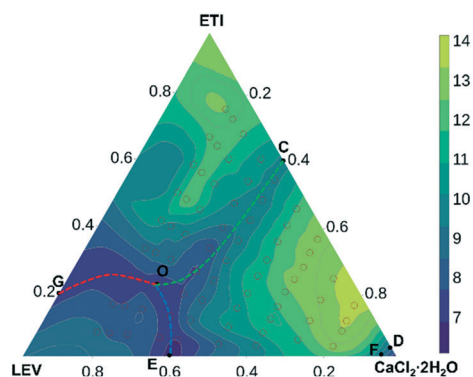


Fig. 8 Dissolution surface of an IQPD for ETI–LEV–CaCl₂·2H₂O–H₂O by application of contour lines. The underlying dots represent the starting position of the overall solid phase. The contour lines show relative mole amount of H₂O required for full dissolution (the total mole of solid starting materials of ETI, LEV and CaCl₂·2H₂O are calculated as 1; yellow is high and purple is low).

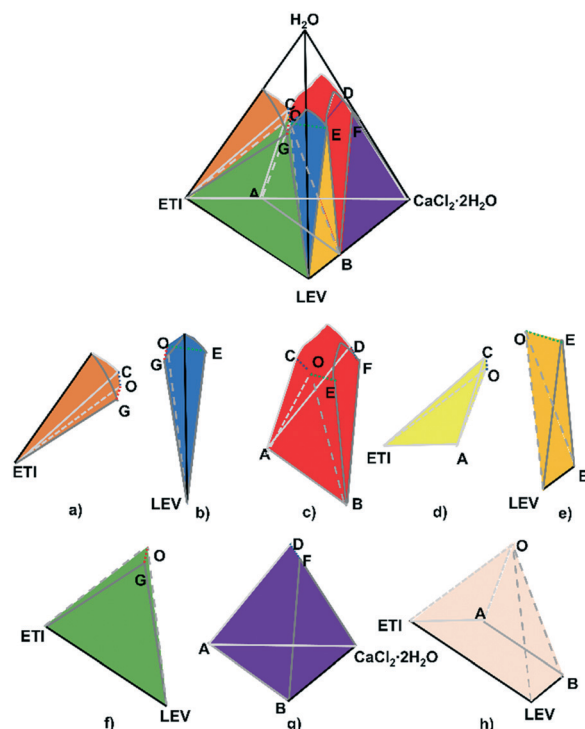


Fig. 9 Up: Stereoscopic IQPD of ETI–LEV–CaCl₂·2H₂O–H₂O system; Down: polyhedrons of various domains composing the full IQPD: a) is ETI + L; b) is LEV + L; c) is ICC3 + L; d) is ETI + ICC3 + L; e) is LEV + ICC3 + L; f) is ETI + LEV + L; g) ICC3 + CaCl₂·2H₂O + L; h) is ETI + LEV + ICC3 + L. Domain of CaCl₂·2H₂O + L is omitted (L represents a liquid phase).

given in Tables S5 and S6[†]). The point on the left edge is the solubility of ETI (0.83 g mL⁻¹) and the point on the right edge is that of LEV (1.05 g mL⁻¹). The enantiopure LEV is about 1.3 times more soluble compared to the racemic compound ETI. The solid line is the liquidus and represents the changing solubility of ETI (or LEV) under varying conditions of overall chiral composition. The eutectic point (point G), where two liquid lines meet, represents the composition of the solution in equilibrium when both ETI and LEV coexist in suspension. The eutectic point lies at a ratio ETI/LEV of 2:8 which means *R*-ETI/*S*-ETI of 1:9, as was already highlighted elsewhere.³³

Into the full diagram

To investigate the full diagram, different isoplethal planes (cut planes, shown in Fig. 7) were constructed, for each keeping the ratio of total organic compound vs. CaCl₂·2H₂O constant. Seven such cut planes were constructed, with a 5:1, 4:1, 3:1, 2:1, 3:2, 1:1, 2:3, 3:7 and 1:4 ratio respectively. To achieve these diagrams, the initial suspensions include 100 mg of organic compound (varying the relative ratio of LEV and ETI) and 13.04 mg, 16.30 mg, 21.73 mg, 32.60 mg, 43.47 mg, 65.20 mg, 97.80 mg, 152.14 mg and 260.81 mg of CaCl₂ respectively (see Table S7[†]). At this stage, water is added to each experimental point up to

complete dissolution. Fig. 7 demonstrates dissolution curves of 3:1 and 1:1 cut planes. The first plane which contains an excess amount of organic compound, clearly shows a eutectic point. No such eutectic is observed for the stoichiometric 1:1 plane. The former is representative of a situation where ETI or LEV is the last phase to dissolve, whereas the latter fully corresponds to the dissolution profile of a solid solution, implying the ICC3 phase to be the last phase to dissolve. Combining the dissolution points of all seven isoplethal planes, a full dissolution surface of the IQPD was constructed as represented in Fig. 8, which shows the amount of water required for full dissolution of a given overall solid composition (data is shown in Table S8†). Point G corresponds to the eutectic of the ETI/LEV mixture in water. Adding $\text{CaCl}_2 \cdot 2\text{H}_2\text{O}$ to the solution, this eutectic point moves to initially lowering the ee, to finally move back to point O. This highlights the fact that solution ee can indeed be impacted by addition of a salt. Overall compositions, along this line correspond to situations where the ETI/LEV mixtures remains the stable phase in suspension up to full dissolution. This diagram also shows that up to an organic compound: $\text{CaCl}_2 \cdot \text{H}_2\text{O}$ ratio of 3:1 the organic phase is the last phase to dissolve, with the isoplethal plane showing a true eutectic (as in Fig. 7 left). As mentioned, for higher concentrations, ICC3 can be stable in suspension to the triphasic region (ETI/LEV/ICC3). Points C, D and E, F represent the solution eutectics of the TPDs shown respectively in Fig. 4 and 5. The eutectic points C and E, representing respectively suspensions of ICC1/ETI, and ICC2/LEV. These points evolve when considering overall ee differing from 0 or 100%. The eutectics move along the C–O and E–O lines, respectively, correspond to solutions for which the final phases to dissolve are respectively ICC3/ETI and ICC3/LEV. Point O represents a true quaternary eutectic representing the solution composition for which all possible solid forms can coexist in suspension (ETI, LEV, ICC3). The region bordered by E–O–C–D–F corresponds to situations where the ICC is the final phase to dissolve.

The data above can then be combined to draw a 3D schematic of the full IQPD. Fig. 9 illustrates the different domains in this IQPD. Polyhedrons a), b) and c) represent biphasic domains: pure ETI, pure LEV or ICC3 in suspension. Polyhedrons d), e), f) and g) are triphasic domains with d), e) and g) representing suspensions of ICC3/ETI, ICC3/LEV or ICC3/ $\text{CaCl}_2 \cdot 2\text{H}_2\text{O}$ respectively; f) represents a suspension of ETI/LEV. The only tetra-phasic domain is h) representing a suspension of ETI/LEV/ICC3 and characterized by a true eutectic invariant supernatant composition. This zone is inside the tetrahedron and difficult to represent. It only reaches the solubility surface through point O.

Due to the formation of the solid solution, this specific system would not be ideal for developing a chiral resolution. However, this work illustrates the importance of the underlying solution thermodynamics, and according to they will pave the way future works in the area of solution based ICC applications. ICCs are gaining interest in pharmaceutical

industry, and it is only a matter of time, before resolution process based on these systems will be developed.

Conclusion

This contribution is the first to investigate the crystallization thermodynamics of an ionic cocrystal system involving chiral species. Focusing on the ETI–LEV– $\text{CaCl}_2 \cdot 2\text{H}_2\text{O}$ – H_2O system, we show how a full isothermal quaternary phase diagram can be obtained, through dissolution experiments. The full quaternary diagram can be represented by a 3D tetrahedron, with its faces comprised of ternary diagrams. To construct the solubility surface, well tetrahedron-chosen isoplethal cut planes were used. The eutectic point of a racemic/enantiopure suspension was shown to vary when a salt is added to the solution. The diagram furthermore confirmed the solid solution nature of the ICC studied in the context of this work. So even though this particular system might not be ideal for the development of novel chiral resolution processes, we do expect this work to pave the way for future ionic cocrystallization based resolution processes.

Conflicts of interest

There are no conflicts to declare.

Acknowledgements

Lixing Song and Fucheng Leng would like to thank the China Scholarship Council (CSC) for financial support. The authors would like to thank the FNRS for financial support (PDR T.0149.19 and PDR T.0262.20).

Notes and references

- 1 E. Grothe, H. Meeke, E. Vlieg, J. H. ter Horst and R. de Gelder, *Cryst. Growth Des.*, 2016, **16**, 3237–3243.
- 2 G. Bolla and A. Nangia, *Chem. Commun.*, 2016, **52**, 8342–8360.
- 3 P. Cerreia Vioglio, M. R. Chierotti and R. Gobetto, *Adv. Drug Delivery Rev.*, 2017, **117**, 86–110.
- 4 R. Shaikh, R. Singh, G. M. Walker and D. M. Croker, *Trends Pharmacol. Sci.*, 2018, **39**, 1033–1048.
- 5 A. Karagianni, M. Malamataris and K. Kachrimanis, *Pharmaceutics*, 2018, **10**, 18–47.
- 6 A. M. Healy, Z. A. Worku, D. Kumar and A. M. Madi, *Adv. Drug Delivery Rev.*, 2017, **117**, 25–46.
- 7 A. R. Buist and A. R. Kennedy, *Cryst. Growth Des.*, 2014, **14**, 6508–6513.
- 8 D. Braga, F. Grepioni and O. Shemchuk, *CrystEngComm*, 2018, **20**, 2212–2220.
- 9 S. BS, *Ars Pharm.*, 2009, **50**, 99–117.
- 10 O. N. Kavanagh, D. M. Croker, G. M. Walker and M. J. Zaworotko, *Drug Discovery Today*, 2019, **24**, 796–804.
- 11 D. D. Bavishi and C. H. Borkhataria, *Prog. Cryst. Growth Charact. Mater.*, 2016, **62**, 1–8.

- 12 F. Grepioni, J. Wouters, D. Braga, S. Nanna, B. Fours, G. Coquerel, G. Longfils, S. Rome, L. Aerts and L. Quere, *CrystEngComm*, 2014, **16**, 5887–5896.
- 13 J. Wouters, F. Grepioni, D. Braga, R. M. Kaminski, S. Rome, L. Aerts and L. Quéré, *CrystEngComm*, 2013, **15**, 8898–8902.
- 14 S. Aitipamula, R. Banerjee, A. K. Bansal, K. Biradha, M. L. Cheney, A. R. Choudhury, G. R. Desiraju, A. G. Dikundwar, R. Dubey, N. Duggirala, P. P. Ghogale, S. Ghosh, P. K. Goswami, N. R. Goud, R. R. K. R. Jetti, P. Karpinski, P. Kaushik, D. Kumar, V. Kumar, B. Moulton, A. Mukherjee, G. Mukherjee, A. S. Myerson, V. Puri, A. Ramanan, T. Rajamannar, C. M. Reddy, N. Rodriguez-Hornedo, R. D. Rogers, T. N. G. Row, P. Sanphui, N. Shan, G. Shete, A. Singh, C. C. Sun, J. A. Swift, R. Thaimattam, T. S. Thakur, R. Kumar Thaper, S. P. Thomas, S. Tothadi, V. R. Vangala, N. Variankaval, P. Vishweshwar, D. R. Weyna and M. J. Zaworotko, *Cryst. Growth Des.*, 2012, **12**, 2147–2152.
- 15 C. Zhang, Y. Xiong, F. Jiao, M. Wang and H. Li, *Cryst. Growth Des.*, 2019, **19**, 1471–1478.
- 16 G. Springuel, K. Robeyns, B. Norberg, J. Wouters and T. Leyssens, *Cryst. Growth Des.*, 2014, **14**, 3996–4004.
- 17 F. George, N. Tumanov, B. Norberg, K. Robeyns, Y. Filinchuk, J. Wouters and T. Leyssens, *Cryst. Growth Des.*, 2014, **14**, 2880–2892.
- 18 S. Iwama, K. Kuyama, Y. Mori, K. Manoj, R. G. Gonnade, K. Suzuki, C. E. Hughes, P. A. Williams, K. D. Harris, S. Veessler, H. Takahashi, H. Tsue and R. Tamura, *Chem. – Eur. J.*, 2014, **20**, 10343–10350.
- 19 G. Springuel and T. Leyssens, *Cryst. Growth Des.*, 2012, **12**, 3374–3378.
- 20 D. Braga, L. Degli Esposti, K. Rubini, O. Shemchuk and F. Grepioni, *Cryst. Growth Des.*, 2016, **16**, 7263–7270.
- 21 O. Shemchuk, B. K. Tsenkova, D. Braga, M. T. Duarte, V. Andre and F. Grepioni, *Chem. – Eur. J.*, 2018, **24**, 12564–12573.
- 22 O. Shemchuk, L. Song, K. Robeyns, D. Braga, F. Grepioni and T. Leyssens, *Chem. Commun.*, 2018, **54**, 10890–10892.
- 23 A. Hovinga Collin, *Pharmacotherapy*, 2001, **21**, 1375–1388.
- 24 A. H. Gouliaev and A. Senning, *Brain Res. Rev.*, 1994, **19**, 180–222.
- 25 L. Song, O. Shemchuk, K. Robeyns, D. Braga, F. Grepioni and T. Leyssens, *Cryst. Growth Des.*, 2019, **19**, 2446–2454.
- 26 L. Lange and G. Sadowski, *Cryst. Growth Des.*, 2015, **15**, 4406–4416.
- 27 M. Liu, C. Hong, Y. Yao, H. Shen, G. Ji, G. Li and Y. Xie, *Eur. J. Pharm. Biopharm.*, 2016, **107**, 151–159.
- 28 D. Ahuja, M. Svärd and Å. C. Rasmuson, *CrystEngComm*, 2019, **21**, 2863–2874.
- 29 S. Kudo and H. Takiyama, *J. Cryst. Growth*, 2014, **392**, 87–91.
- 30 Y. Tong, Z. Wang, L. Dang and H. Wei, *Fluid Phase Equilib.*, 2016, **419**, 24–30.
- 31 D. M. Croker, M. E. Foreman, B. N. Hogan, N. M. Maguire, C. J. Elcoate, B. K. Hodnett, A. R. Maguire, Å. C. Rasmuson and S. E. Lawrence, *Cryst. Growth Des.*, 2012, **12**, 869–875.
- 32 L. Song, K. Robeyns and T. Leyssens, *Cryst. Growth Des.*, 2018, **18**, 3215–3221.
- 33 B. Harmsen and T. Leyssens, *Cryst. Growth Des.*, 2017, **18**, 441–448.
- 34 G. Springuel, L. Collard and T. Leyssens, *CrystEngComm*, 2013, **15**, 7951–7958.
- 35 F. George, B. Norberg, K. Robeyns, J. Wouters and T. Leyssens, *Cryst. Growth Des.*, 2016, **16**, 5273–5282.